International Journal of Heat and Mass Transfer 216 (2023) 124605

Contents lists available at ScienceDirect

International Journal of Heat and Mass Transfer

journal homepage: www.elsevier.com/locate/ijhmt

Surface evaporation enhancement using porous metasurfaces: 3-D multiscale, open-system wick evaporators

Yuki Kameya [a,*], Yuya Takahashi [a], Massoud Kaviany [b]

[a] Department of Mechanical Engineering, Chiba Institute of Technology, Narashino, Japan
[b] Department of Mechanical Engineering, University of Michigan, Ann Arbor, MI, 48109, United States

ARTICLE INFO

Keywords:
Porous metasurface
Surface evaporation
3-D multiscale wick
Irrigating artery
Capillary-viscous limit
Evaporation enhancement

ABSTRACT

In open-system water-vapor production by direct heat supply, wick evaporators are promising for efficient use of the supplied heat. However, designing a suitable wick structure for achieving high evaporator performance had proven challenging. Here, novel, high-performance porous metasurfaces (unit-cell based capillary structures) are designed, fabricated and tested, using sintered copper powder. In addition, the wicks optimized for yet higher performance are presented. Vertically placed wicks are partially submerged in a pool of water, while heated through a copper substrate by Joule heating. The baseline wick is a monolayer wick, and three different particle diameters (78, 100, and 130 μm) are used. The next variations are bilayer wicks which improve the particle packing and the maximum capillary pressure. The most improvement is achieved by adding strips of capillary arteries (1 mm thick and 1 mm wide, with an interartery gap of 1 mm) on the monolayer. These unit-cell based 3-D porous metasurfaces allow for tailoring the surface design to achieve an optimal thermal-hydraulic performance. Analyses of the wick capillary-viscous dryout limit and the extended-surface heat transfer predict the performance of the fabricated wicks under the test conditions. Overall, an evaporation efficiency of unity and an evaporation enhancement by 50% are recorded.

1. Introduction

Water vapor generation is widely utilized, for example, in moist-air or process steam production with solar thermal energy, using tubular humidifier [1], flat-plate solar collector [2], high-vacuum insulated solar collector [3], steam drum with immersed heat pipes [4], or solar-still basin [5]. The efficient use of thermal energy with minimal heat loss has been explored [6], and evaporators have been developed to adapt to the individual operating conditions of applied systems [7]. Water evaporation via local heating of the air-water interface has an advantage over conventional bulk heating-based evaporation [8]; this approach has been demonstrated using laser-processed cotton paper [9], polytetrafluoroethylene membrane with reduced graphene oxide [10], and biomass-based hydrogel [11]. Thin film evaporation is a potential approach for efficient vaporization of liquids [12]. A thin liquid film spreading over a heated solid surface has a low thermal resistance, which leads to evaporation at the liquid-gas interface with moderate superheat of the solid surface. To sustain continuous thin film evaporation, passive liquid feeding using a capillary wick is a promising technique [13].

Wick evaporators enable the expansion of liquid-gas interfacial areas (i.e., evaporation surfaces) by capillary action and support the formation of meniscus and the creation of thin liquid film on porous solid matrices; these have included grooved heat pipe [14], heat spreader [15], planar vapor chamber [16], and microgravity cooling device [17]. These in turn result in heat loss reduction, i.e., the effective spreading of the supplied heat to the evaporation area. Copper wicks have been used because of excellent heat transfer properties and capillary performance, as well as their compatibility with water; for example, laser-machined lattice-pattern wick [18], micro-groove channel wick [19], and electrodeposited dendritic wick [20]. Wicks with liquid-supply arteries can assist in spreading water over a larger evaporation area [21,22]. The liquid flow through wicks is enabled by capillary pressure, while viscous drag limits the spreading of liquid. The hydrodynamic capillary-viscous limit refers to the balance between the capillary pressure and viscous drag in liquid flow through wicks [15,23]. Heat transfer is governed by the conduction path through the substrate and wick to the evaporation surface. Therefore, the evaporation surface temperature (and vapor partial pressure) and the heat flow rate are affected by the wick design with the arteries acting as an extended surface. This combined thermal-hydraulic behavior determines the evaporation efficiency and

* Corresponding author.
E-mail addresses: yuki.kameya@it-chiba.ac.jp, yuki.kameya.jp@gmail.com (Y. Kameya).

https://doi.org/10.1016/j.ijheatmasstransfer.2023.124605
Received 20 June 2023; Received in revised form 21 July 2023; Accepted 12 August 2023

Nomenclature

A	area (m^2)
d	diameter (m)
g	gravitational acceleration (m/s^2)
h	height (m), enthalpy (J/kg), heat transfer coefficient (W/m^2-K)
k	thermal conductivity (W/m-K)
K	permeability (m^2)
L	length (m)
$\dot{M}$	mass flow rate (kg/s)
$\dot{m}$	mass flux ($kg\ m^{-2}\ s^{-1}$)
N	integer number (-)
Pe	Péclet number, $u_l\delta_a/\alpha_l$ (-)
Q	heat flow rate (W)
q	heat flux (W/m^2)
R	thermal resistance (K/W)
r	radius (m)
T	temperature (K)
u	velocity (m/s)
W	width (m)

Greek symbols

α	thermal diffusivity (m^2/s)
δ	length (m)
Δ	difference (-)
ε	porosity (-)
η_e	evaporation efficiency (-)
η_f	fin efficiency (-)
μ	dynamic viscosity (Pa-s)
ρ	density (kg/m^3)
σ	surface tension (N/m)

Subscripts

a	artery
at	artery tip
$base$	base area
c	capillary, curvature, cross-sectional
cv	capillary-viscous
e	evaporation
f	fin, fluid
g	interartery gap, gas
l	liquid
lg	liquid-gas phase change
m	monolayer
max	maximum
min	minimum
p	particle
s	submerged, surface, solid
∞	ambient

influences the evaporation rate.

In an open-system evaporator design, the evaporation efficiency is defined as the fraction of supplied heat that results in evaporation. Evaporator inefficiency arises as heat losses, for example heat flow to any surface not covered or supplied with liquid. Wick-covered surfaces can irrigate the surface effectively and increase the evaporation efficiency. Hence, designing a suitable wick structure is essential to achieve a desirable evaporator performance.

Unit-cell based metasurfaces are engineered for specific surface functions, and have been used in tailoring surface reflection, transmission and absorption properties of electromagnetic and sound waves [24], in control and enhancement of the flow-boiling crisis [25], and in optimization of dropwise condensation of biphilic surfaces [26]. The concept of a metasurface is applicable to wick evaporators. Unit-cell based structures offer flexibility in the design of evaporators, allowing for customization according to the required dimensions and specifications of the applied system. To date, the potential of porous metasurfaces for open-system wick evaporators has not been explored. Establishing a design strategy for such metasurfaces and its demonstration are desirable for advancing practical evaporators.

In this study, we propose 3-D porous metasurfaces for enhanced surface evaporation, using sintered copper-powder unit-cell based wicks on a copper substrate to achieve a water evaporation efficiency of unity in an open system. To the best of our knowledge, the evaporator wicks proposed here are new, novel evaporation-enhancing surface structures. Experimental demonstration and theoretical analysis of the 3-D wick evaporators provide new insights into the open-system vapor production processes. The objectives of this study are to demonstrate the evaporation performance of these proposed wicks and provide the fundamentals allowing for analytic prediction of this performance. The organization of this article is as follows. Section 2 introduces the multiscale structures of wicks and discusses the capillary-viscous limit of evaporation flux. Section 3 describes the fabrication process and the geometrical parameters of the prepared wicks, followed by Section 4, which describes the characteristics of the fabricated wicks. Section 5 describes the experimental setup and procedure to evaluate wick performances for water evaporation. Section 6 presents the experimental results, the interpretation of the results, and prospects for 3-D multiscale wicks. Finally, Section 7 presents the concluding remarks.

2. Evaporation porous metasurface unit cell and capillary-viscous limit

Fig. 1(a) shows a schematic of open-system evaporation (water evaporating in air), and Fig. 1(b) shows the unit-cell schematic of a 3-D wick. An otherwise quiescent pool of water is used to generate vapor in an open system; such pool evaporation is generally used in applications where a water reservoir is heated for vapor production [4]. In our set-up, the vertically placed wick (the width W and the length L) is partially submerged in the water pool; L_s is the submerged length in the pool, and L_e is the evaporation length of the wicked surface [i.e., the wick length used for evaporation, as shown in Fig. 1(a)]. Water continuously flows through the wick, rises owing to capillary action, and vaporizes into the air from the wetted wick surface. The wick is made of sintered submillimeter copper particles so that its porous structure produces sufficient capillary pressure. The monolayer covers the entire plain surface of the copper substrate, and the capillary arteries are placed on top of monolayer. The monolayer and vertical artery structures comprise the multiscale 3-D wick; the artery dimensions, namely the width W_a, length δ_a, and interartery gap W_g are in the order of millimeters. The capillary rises through the monolayer and arteries extend the evaporation area. Additionally, the interartery space allows for an extra capillary rise h_a (i.e., the macroscopic interartery meniscus). The monolayer supports thin liquid film evaporation. The arteries not only assist with irrigation to prevent monolayer dryout, but also work as fins (forming an extended surface) for enhancing water evaporation. The unit cell is defined as shown by the dashed line in Fig. 1(b), reflecting the periodic arrangement of the arteries. The fabrication process and dimensions of the tested wicks are described in Section 3.

The capillary-viscous dryout limit for the unit cell of the 3-D wick is described here. Using the maximum capillary pressure $p_{c,max}$ of the monolayer wick, the maximum mass flow rate through the wick is controlled by the capillary suction and retarding viscous drag. We start with the Darcy law [27] and the Young-Laplace equation [28],

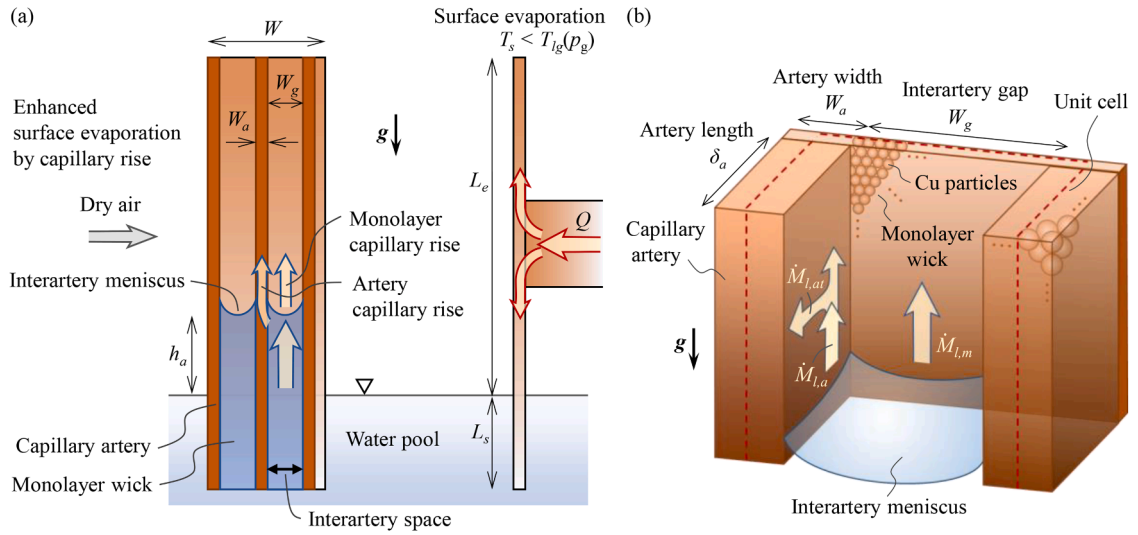

Fig. 1. (a) Schematic of the partially submerged evaporation wick utilizing vertical arteries for further capillary-rise assist (shown as the interartery capillary rise h_a) and enhanced evaporation area. The submerged wick length varies during evaporation. The geometric parameters are also shown. (b) Schematic of capillary arteries and interartery space showing the mass flow rates of the liquid used in predicting the wick capillary-viscous evaporation flux limit.

$$-\nabla p = \frac{\mu_l}{K}\boldsymbol{u}_l, \tag{1}$$

$$p_{c,\max} = \frac{2\sigma}{r_{c,\min}}, \tag{2}$$

where p is the pressure, μ_l is the viscosity of the liquid, K is the permeability, $\boldsymbol{u}_l$ is the liquid flow velocity, σ is the liquid surface tension, and $r_{c,min}$ is the minimum radius of curvature. The mass flux though monolayer $\dot{m}_m$ is related with the flow velocity as $\dot{m}_m = \dot{M}_{l,m}/A_m = \rho_l u_l$, where $\dot{M}_{l,m}$ is the liquid mass flow rate through monolayer, A_m is the cross-sectional area of the monolayer ($A_m = W\langle d_p\rangle$), and ρ_l is the liquid density. Using the wick evaporation length L_e, and noting that evaporation decreases the liquid mass flow rate (assuming linearly) along the wick, we have

$$\frac{p_{c,\max} - \rho_l g L_e/2}{L_e/2} = \frac{\mu_l}{K_m}\frac{\dot{M}_{lg-cv}}{\rho_l A_m}, \tag{3}$$

where g is the gravitational acceleration, and $\dot{M}_{lg\text{-}cv}$ is the evaporation rate assuming the dryout limit ($\dot{M}_{lg\text{-}cv} = \dot{M}_{l,m}$). Neglecting the gravity effect, the capillary-viscous evaporation flux limit for the monolayer is

$$\dot{m}_{lg-cv} = \frac{4\sigma(T_s)\rho_l(T_s)}{\mu_l(T_s)L_e}\frac{K_m}{r_{c,\min}}\frac{A_m}{A_{base}}, \quad T_s > T_\infty. \tag{4}$$

Here the base area A_{base} ($= WL$) is used to be consistent with experimental values described later. We assume the water properties at the wick surface temperature T_s, which is higher than the ambient temperature T_∞.

Regarding the arteries, we consider the mass flow rate through each artery $\dot{M}_{l,a}$ and assume the dryout limit ($\dot{M}_{lg\text{-}cv} = \dot{M}_{l,a}$). The capillary-viscous evaporation flux limit for the arteries is

$$\begin{aligned}\dot{m}_{lg-cv} &= \frac{4\sigma(T_s)\rho_l(T_s)}{\mu_l(T_s)(L_e - h_a)}\frac{K_a}{r_{c,\min}}\frac{A_a}{A_{base}} \\ &= \frac{4\sigma(T_s)\rho_l(T_s)}{\mu_l(T_s)(L_e - h_a)}\frac{K_a}{r_{c,\min}}\frac{W_a}{W_a + W_g}\frac{\delta_a}{L}, \quad T_s > T_\infty.\end{aligned} \tag{5}$$

Here we used the relations $A_a = W_a\delta_a N_a$ and $N_a = W/(W_a + W_g)$. Also, we assume the interartery meniscus height as $h_a = 2\sigma\cos\theta_c/\rho_l g W_g$ [29].

Eq. (5) suggests that the evaporation rate can increase with the artery length because of the extended evaporation surface area. On the other hand, the dryout of the artery tip would occur during enhanced evaporation, limiting the maximum evaporation rate. Using the artery length δ_a, and noting that evaporation decreases the liquid mass flow rate (assuming linearly) along the artery length, we have

$$\frac{p_{c,\max}}{\delta_a/2} = \frac{\mu_l}{K_a}\frac{\dot{M}_{l,at}}{\rho_l W_a L_e}, \tag{6}$$

where $\dot{M}_{l,at}$ is the liquid mass flow rate through each artery in the direction of the artery tip. The capillary-viscous evaporation flux limit for arteries per unit base area is

$$\dot{m}_{lg-cv} = \frac{4\sigma(T_s)\rho_l(T_s)}{\mu_l(T_s)\delta_a}\frac{K_a}{r_{c,\min}}\frac{W_a}{W_a + W_g}\frac{L_e}{L}. \tag{7}$$

In contrast to Eq. (5), the evaporation rate decreases with increases in the artery length. The presented model of the capillary-viscous limit is based on the same fundamentals (i.e., Darcy law and Young-Laplace equation) similar to the treatment reported for the multi-artery heat pipe spreader [15,28]. The unique features specific to the 3-D wick structures used in this study are subject of this experimental work. The derived equations are used and discussed in conjunction with the experimental results in Section 6.

3. Porous metasurface fabrication

We used commercial Cu powder with a nominal particle diameter of 100 μm and 99.8% purity (Nilaco, Japan). Sieving was performed to control the particle size distribution; two stainless-steel sieves with 90 and 106 μm openings (conforming to ISO 3310-1 criteria) were used to obtain three size ranges. By means of electron microscopy, we determined the mean particle diameters $\langle d_p\rangle$ as 78, 100, and 130 μm.

Using the sieved Cu powder, wicks were fabricated on a Cu substrate with dimensions of 50 mm (L) × 10 mm (W) and a thickness of 0.5 mm. The basic fabrication methods were the same as those described in [30,31]. The sieved Cu powder was spread over the water–air interface to form the monolayer particle arrangement [32], which was then transferred onto a Cu substrate. Next, the particles were sintered in an electric furnace at 800 °C with a constant flow of gaseous nitrogen and hydrogen mixture; thus, the monolayer wicks were obtained. For the bilayer wick structure, the above fabrication step for the monolayer was repeated twice. To fabricate the artery structures, a graphite mold with the desired pattern was machined. Then the graphite mold was filled with

Cu particles, over the monolayer or plain substrate, and then sintered to obtain samples with the artery structures. The structural characteristics of the prepared wicks are summarized in Table 1. Also, a plain substrate (with no wick structure) was used as a reference to evaluate the evaporation performance of the wicks.

Fig. 2 shows scanning electron microscopy (SEM) micrographs of a monolayer wick with $\langle d_p \rangle = 78$ μm (Wick 1). The monolayer was fabricated as intended, so the pile of particles could be neglected [Fig. 2(a)]. The particles covered the substrate surface up to the edge, as shown in the side view [Fig. 2(b)]. Other monolayer and bilayer samples were also observed, and their structures were validated.

The arteries consisted of particles with a mean diameter of $\langle d_p \rangle = 130$ μm to achieve high permeability (Fig. 3). The dimensions and positions of the arteries were controlled using a graphite mold during particle sintering. The artery width W_a and length δ_a were both 1 mm, and the vertical length was 50 mm; the arteries were placed parallel to the long edge of the substrate. The number of arteries N_a was 5 or 3 [Fig. 3(a,b)]. When $N_a = 5$ and 3, the gap between the arteries W_g was 1 mm (Wicks 5 and 6) and 3 mm (Wick 7), respectively. Wicks 5 and 7 had a monolayer of $\langle d_p \rangle = 78$ μm beneath the arteries; after monolayer was sintered uniformly over the substrate, the arteries were added [Fig. 3(c)]. Wick 6 had no monolayer; the arteries were added directly to a plain substrate.

4. Characteristics of the fabricated metasurfaces

The monolayer wick permeability K_m, which depends on the particle diameter and porosity, is estimated using the relevant existing data. This is shown in Fig. 4(a), for two particle diameters used here, along with the literature data [15,33]. Hwang et al. reported $K_m = 4.68$ μm^2 for a monolayer wick of $\langle d_p \rangle = 60$ μm [15]. Albu et al. reported $K_m = 20.4$ and 70.5 μm^2 for monolayer wicks of $\langle d_p \rangle = 100$ and 200 μm, respectively [33]. Based on these values, we determined the permeabilities of monolayer wicks fabricated in this study as follows: $K_m = 11.4$, 20.4, and 33.8 μm^2 for monolayer wicks of $\langle d_p \rangle = 78$, 100 and 130 μm, respectively. Then, we used the Carman-Kozeny equation to estimate the permeability of the arteries [27]. Assuming a porosity of 0.4 (random packing of spherical particles), we determined $K_a = 16.7$ μm^2.

The minimum radius of curvature for water meniscus $r_{c,min}$ was also estimated for each monolayer wick. Liquid suction experiments provide the relation $r_{c,min} = 0.54\ \langle d_p \rangle$ [33]. Hence, we determined $r_{c,min} = 42.1$, 54.0, and 70.2 μm for monolayer wicks of $\langle d_p \rangle = 78$, 100, and 130 μm, respectively, as shown in Fig. 4(b). These values were used to estimate the maximum capillary pressure $p_{c,max}$ through the Young–Laplace equation: $p_{c,max} = 2\sigma/r_{c,min}$, where σ is the surface tension of water.

5. Experiments

The performances of the prepared wicks were evaluated by measuring their thermal resistances and evaporation rates. The backside of each wick was connected to a rectangular copper bar with a cross-sectional area of 8 × 8 mm^2 (i.e., the heating area A_h) using solder paste (see Fig. A.1). The other edge of the copper bar was soldered onto a heater block with an embedded cartridge heater CHA1152 (Kashima, Japan). Three thermocouples (Type T) were embedded in the copper bar to determine the heat flow rate; the copper bar was insulated to assume the one-dimensional Fourier law. The use of the copper bar in which thermocouples were embedded offered a simple approach to transfer heat from a heater and to measure the input heat. This approach has been commonly used in the investigation of evaporation surfaces [15,34,35]. The evaporator surface temperature T_s was determined by extrapolation of the temperature distribution measured along the copper bar.

Table 1
Structural characteristics of various porous metasurface wicks fabricated and tested.

Wick #	Structure	$\langle d_p \rangle$ (μm)
Wick 1	Monolayer	78
Wick 2	Monolayer	100
Wick 3	Monolayer	130
Wick 4	Bilayer	78/130[a)]
Wick 5	Five arteries on a monolayer	78/130[b)]
Wick 6	Five arteries on a plain substrate	130
Wick 7	Three arteries on a monolayer	78/130[b)]

[a)] $\langle d_p \rangle = 78$ μm is for the first (bottom) layer.
[b)] $\langle d_p \rangle = 78$ μm is for the monolayer; $\langle d_p \rangle = 130$ μm is for the arteries.

The wick was partially submerged in a pool of water, as shown in Fig. 1. The surface area of the water pool was 57 × 57 mm^2, and the depth was 27.6 mm. The water pool was fully filled with deionized water and placed on an electronic balance (AUW-120D; Shimadzu, Japan). The water mass was measured to determine the rate of water reduction due to evaporation. The submerged length L_s and evaporation length L_e were 24 and 26 mm, respectively, at the beginning of each test.

The voltage applied to the cartridge heater was increased stepwise using a voltage regulator V-130-5 (Yamabishi Denki, Japan); the voltage and current were monitored to evaluate the input power using a digital multimeter GDM-8342 (GW Instek, Taiwan). A data logger GL240 (Graphtec, Japan) was used to collect experimental data with time. The heat flux was determined at a steady state. The experiments were performed under atmospheric pressure. Dry nitrogen gas was supplied to the sample surface to reduce the mass transfer resistance. The heat loss from the back of the wick substrate is due to natural convection to air, which is shown to be negligibly small (Appendix A) compared with the evaporation heat flow rate. The experiments were repeated at least three times for each sample to ensure reproducibility; the representative one set of data is shown in the following section.

Using the uncertainties in the temperature (±0.5 °C) and the thermocouple location (±0.4 mm), we estimated the uncertainty propagation including the errors in the linear regression of temperature gradient [36], in determining the heat flux and thermal resistance. An uncertainty analysis of the experimental results is presented in Appendix B. The maximum uncertainty in q is 30% (occurring for the plain surface) in A_hR is 53% (occurring at very low heat flux). Regarding the water mass loss measurement, the uncertainty is ±0.02 mg which is considered having negligible effect on the evaporation flux.

6. Results and discussion

6.1. Experimental evaluation of the wicks

The thermal resistance variation with respect to the heat flux for each sample is shown in Fig. 5. The specific thermal resistance A_hR is defined as the wick superheat divided by the heat flux: $\Delta T/q$. The reduction of thermal resistance with increasing heat flux is due to the receding meniscus in wicks, as reported in [15]. The lower thermal resistance corresponds to an enhanced thin-film evaporation. This reduction in the thermal resistance is observed for every wick in the low heat flux range of $q < \sim 15$ W/cm^2.

The thermal resistances of the monolayers, which are indicated by the dashed lines in Fig. 5(a-c), are predicted using the heat transfer model [15] with the mean particle diameters in this study; the agreement supports the validity of the test results. As the heat flux increases, different behaviors are observed depending on the wick structure. Regarding the monolayers and bilayers, the thermal resistance increases after reaching its minimum [Fig. 5(a-d)]. This is due to the partial dryout of the wick surface. The arteries remedy this, preventing any increases in thermal resistance up to $q \sim 40$ W/cm^2 [Fig. 5(e-g)]. The plain substrate shows no remarkable change in the thermal resistance because of the absence of a wick structure [Fig. 5(h)].

The evaporation flux $\dot{m}_{lg}$ was evaluated as the water evaporation rate per unit base area of the wick. This was determined from the mass reduction rate of the water pool $\dot{M}_{lg}$ and the substrate area as:

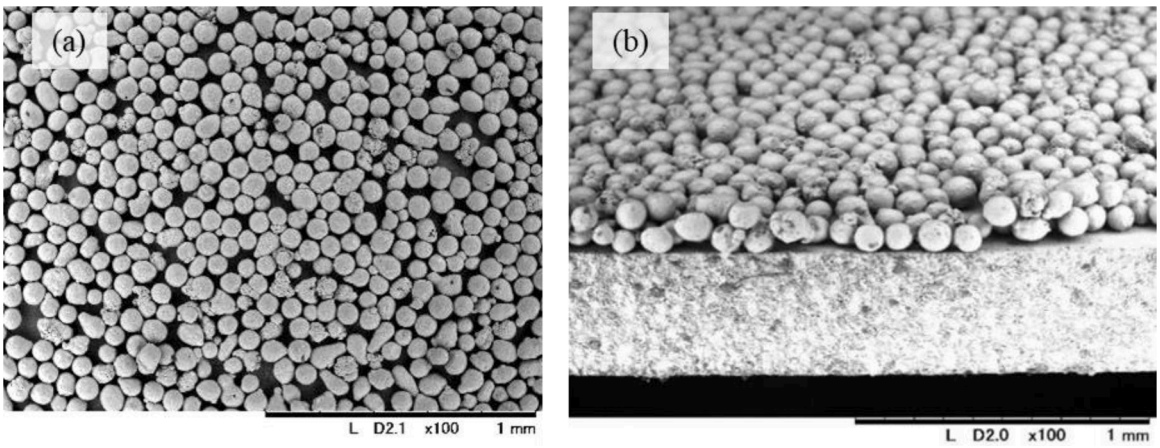

Fig. 2. SEM micrographs of Wick 1: (a) top view and (b) side view.

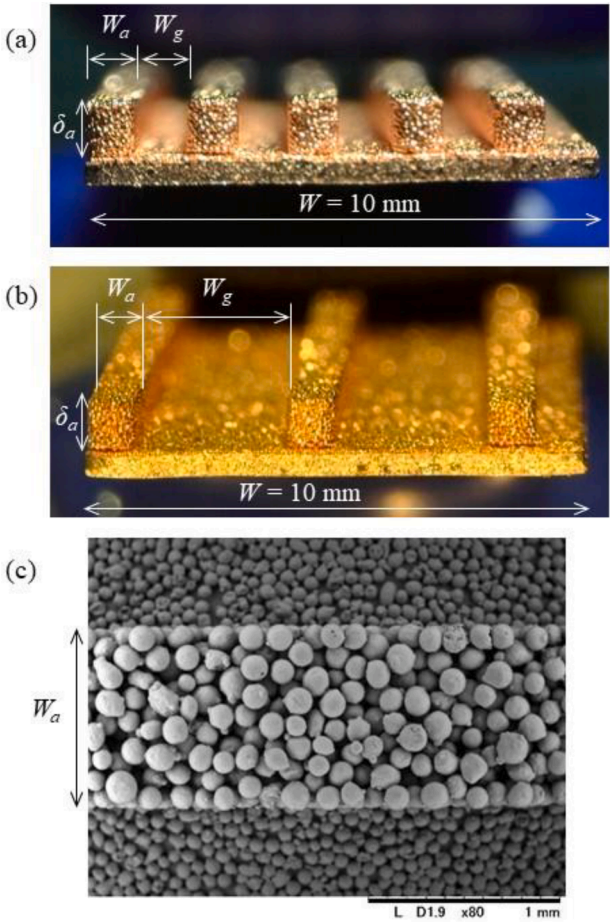

Fig. 3. Photographs of the lower side of the monolayer wicks with (a) five arteries (Wick 5) and (b) three arteries (Wick 7), along with (c) SEM micrograph of a capillary artery. The monolayer wick with smaller particles is also observed.

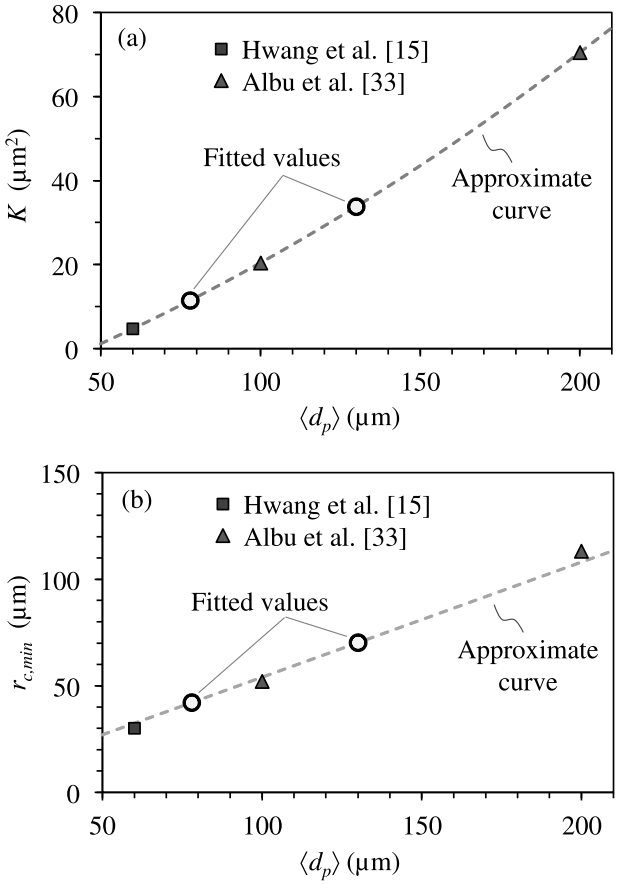

Fig. 4. Physical parameters of monolayers: (a) the variations of the permeability with the average particle diameter, and (b) the variations of the minimum radius of curvature for water meniscus with respect to the average particle diameter. Data from [15,33] are shown by the black symbols. The curve fit is shown by the dashed line. The monolayer wick K and $r_{c,min}$, for $\langle d_p \rangle$ = 78 and 130 μm, are indicated by the circle symbols.

$$\dot{m}_{lg} = \frac{\dot{M}_{lg}}{A_{base}}, \tag{8}$$

where A_{base} is the base area of the wick (50 × 10 mm^2). The results are summarized in Fig. 6, where the evaporation flux is plotted with respect to the temperature difference between the wick surface and ambient. The ambient temperature was nearly constant at 22 °C, and we can assume the influence of ambient humidity was negligible because of constant purge with dry nitrogen gas flow. Compared with the plain substrate that corresponds to the heating of the water pool surface [Fig. 6(h)], all the wicks effectively enhanced water evaporation. The monolayers and bilayer wicks show rather limited evaporation fluxes compared to those of the wicks with arteries because of the partial dryout at high heat flow rates.

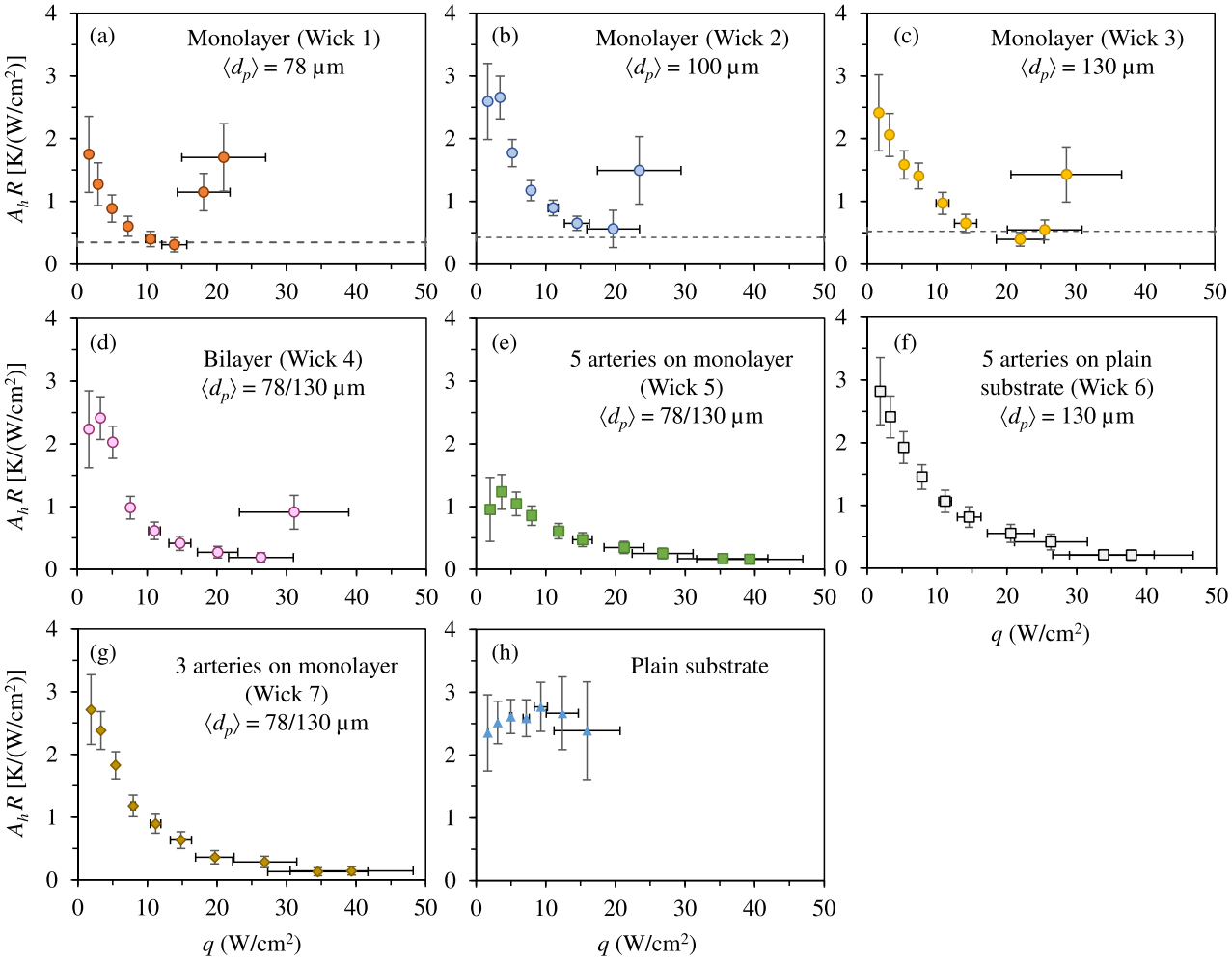

Fig. 5. Variations of the specific thermal resistance with respect to the heat flux for various wicks (a–g) and the plain substrate (h). The resistance decreases with the heat flux, till dryout is reached. Not all cases were tested up to the dryout limit. The error bars represent the estimated uncertainties (Appendix B).

The wicks expand the evaporation surface and support thin-film evaporation, so that the input heat effectively evaporates water. To demonstrate this, we determined the evaporation efficiency as follows:

$$\eta_e = \frac{\dot{M}_{lg}\Delta h_{lg}}{Q}, \tag{9}$$

where Q is the heat flow rate ($A_h q$), and Δh_{lg} is the enthalpy of vaporization. The results are shown in Fig. 7. Compared with the plain substrate, whose efficiency is below 0.5 [Fig. 7(h)], all the wicks are effective in using heat to efficiently evaporate water. The wicks exhibit higher evaporation efficiencies as the heat flow rate increases. The bilayer wick (Wick 4) shows a higher efficiency than that of the monolayer wicks [Fig. 7(d)]. The bilayer wick allows for the improvement of particle packing by making up for defects in monolayer, resulting in an enhanced maximum capillary pressure. Although the bilayer wick has these advantages, the range of its heat flow rate is limited compared with that of the wicks with capillary arteries. It should be noted that the efficiency exhibited by Wick 5 almost reaches unity [Fig. 7(e)]. The efficiency of unity indicates that the supplied heat is entirely utilized for evaporation (i.e., no heat loss), so Wick 5 has an excellent performance (under the testing conditions).

To understand the effect of the 3-D structures on the wick evaporation performance, we compare the results as shown in Fig. 8. The role of the monolayer is examined in Fig. 8 (a); Wick 6 (five arteries on a plain substrate) is compared with Wicks 1 (monolayer) and 5 (five arteries on a monolayer). The evaporation efficiency (repeated from Fig. 7) and wick surface temperature (approximate curve) are plotted with respect to the heat flow rate. Wick 1 entered the phase of partial dryout before reaching $T_s = 100$ °C, and the evaporation efficiency was less than 0.9. Wick 5 reached 100 °C without dryout and achieved an efficiency of nearly unity. Based on these observations, the heat loss at low heat flow rates ($Q < 10$ W) was attributed to heat escaping to the gas phase because the water temperature at the wick surface had been lower than the saturation temperature at 1 atm. The surface temperature of Wick 6 was between those of Wicks 1 and 5, and the evaporation efficiency was lower than that of Wick 5 at high heat flow rates ($Q > 10$ W). Although water was vertically transported through the arteries by the capillary pressure, there was no mechanism for lateral water spreading in the interartery spacing of Wick 6. The evaporation enhancement was limited for Wick 6 at $T_s > 100$ °C, differing from that for Wick 5. Hence a monolayer at the base of arteries is essential for achieving effective evaporation enhancement at high heat flow rates.

The influence of the interartery gap is examined in Fig. 8(b); Wick 7 (three arteries on a monolayer) is compared with Wicks 1 and 5. The interartery gap of Wick 7 ($W_g = 3$ mm) was wider than that of Wick 5 ($W_g = 1$ mm); this suggests the lower interartery capillary rise and the longer lateral length of water spreading to cover the interartery monolayer. Also, the wick surface temperature of Wick 7 remained below 100 °C. These factors hindered the evaporation enhancement, presumably leading to a lower evaporation efficiency. In addition, Wick 7 had only two unit cells, whereas Wick 5 had four unit cells. Therefore, the edge effects could have potentially influenced a comprehensive

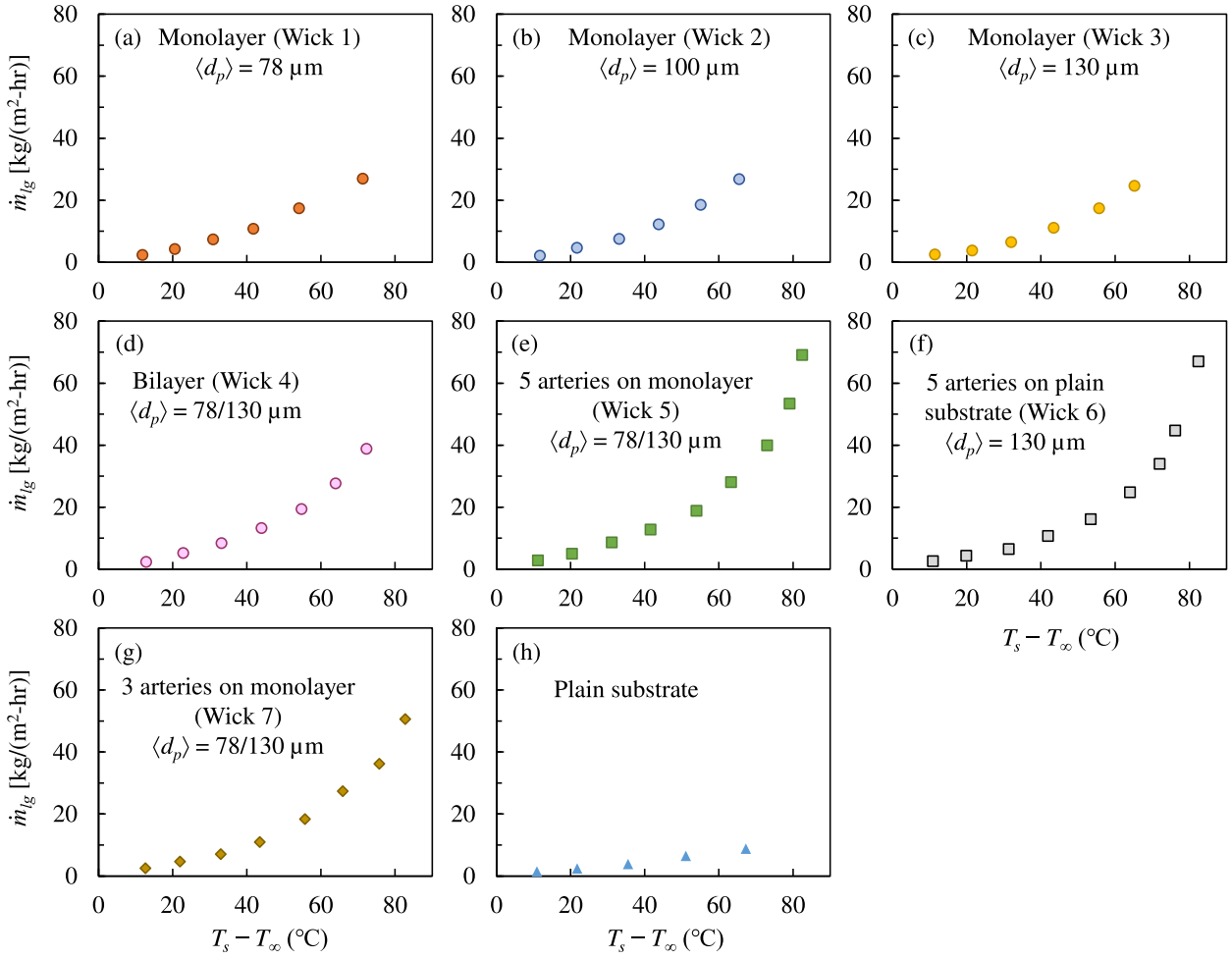

Fig. 6. Variations of the evaporation flux with respect to the difference between the substrate surface and ambient temperatures, for various porous metasuface wicks (a–g) and the plain substrate (h). The ambient temperature was nearly constant at 22 °C.

comparison between the wicks. Overall, a smaller interartery gap appears to be favorable for evaporation enhancement.

The open-system evaporation covered in literature varies based on the system configuration, energy supply (direct solar irradiation, heating with heat pipes, etc.), and conditions (e.g., [4,5]). This study proposes a novel approach to enhancing the surface evaporation, using porous metasurfaces, which offers a fundamental technique for vapor production with direct heat supply. The performance improvement was demonstrated by comparing the seven metasurfaces with the plain substrate (no wick). It is expected that the proposed porous metasurfaces will be incorporated in existing and emerging vapor-production systems.

6.2. *Capillary-viscous evaporation flux limit*

To elucidate the wick performance observed in the experiment, we examined the wick capillary-viscous limit described in Section 2. To demonstrate the effect of the 3-D wick structure with arteries, here we discuss the results of two wicks, namely Wicks 1 and 5. The capillary-viscous evaporation flux limits are plotted as a function of the surface temperature, $T_s - T_\infty$, in Fig. 9 along with the experimental data, which are the same shown in Fig. 6.

Fig. 9(a) presents the result for Wick 1 (monolayer wick). The capillary-viscous mass flux limit is predicted using Eq. (4). The wick evaporation length is assumed to be $L_e = 38$ mm, using the average of the initial and final values in the test, which are 26 and 50 mm, respectively. Using a constant, average evaporation height allows for the steady-state, one-dimensional analysis of Section 2, simplifying an otherwise transient phenomena including the water level variation and the receding macroscopic meniscus. Further model improvement is possible using transient analysis, and this is left for future work. The water properties depend on the temperature, as indicated in Eq. (4), with the predicted mass flux limit increasing with the temperature. The evaporation mass flux obtained in the experiment also increases with temperature and approaches the predicted limit at high temperatures. The closeness of the evaporation flux to the limit is supported by the increase of thermal resistance indicating the initiation of partial dryout [Fig. 5(a)]. Hence, the capillary-viscous limit determines the maximum evaporation flux of the monolayer wick.

Fig. 9(b) shows the result for Wick 5 (monolayer with five arteries). The capillary-viscous evaporation flux limit is predicted using Eq. (5). In Section 2, the liquid flow along the artery length was also discussed, and Eq. (7) was derived. However, the capillary-viscous limit predicted by Eq. (7) is much larger than that predicted by Eq. (5) for the structural parameters of this wick; thus Eq. (5) dominates the upper limit. Additionally, the predicted capillary-viscous evaporation flux limit is much higher than the measured result for Wick 5. We point to the simplifying assumptions made, including the relation for the interartery meniscus height, in arriving at Eq. (5). However, this may not suffice to explain the large difference.

The predicted evaporation flux limit of Wick 5 is significantly higher than that of Wick 1 which is based on Eq. (4). Three factors contribute to this significant increase. First, the cross-sectional area of the liquid flow

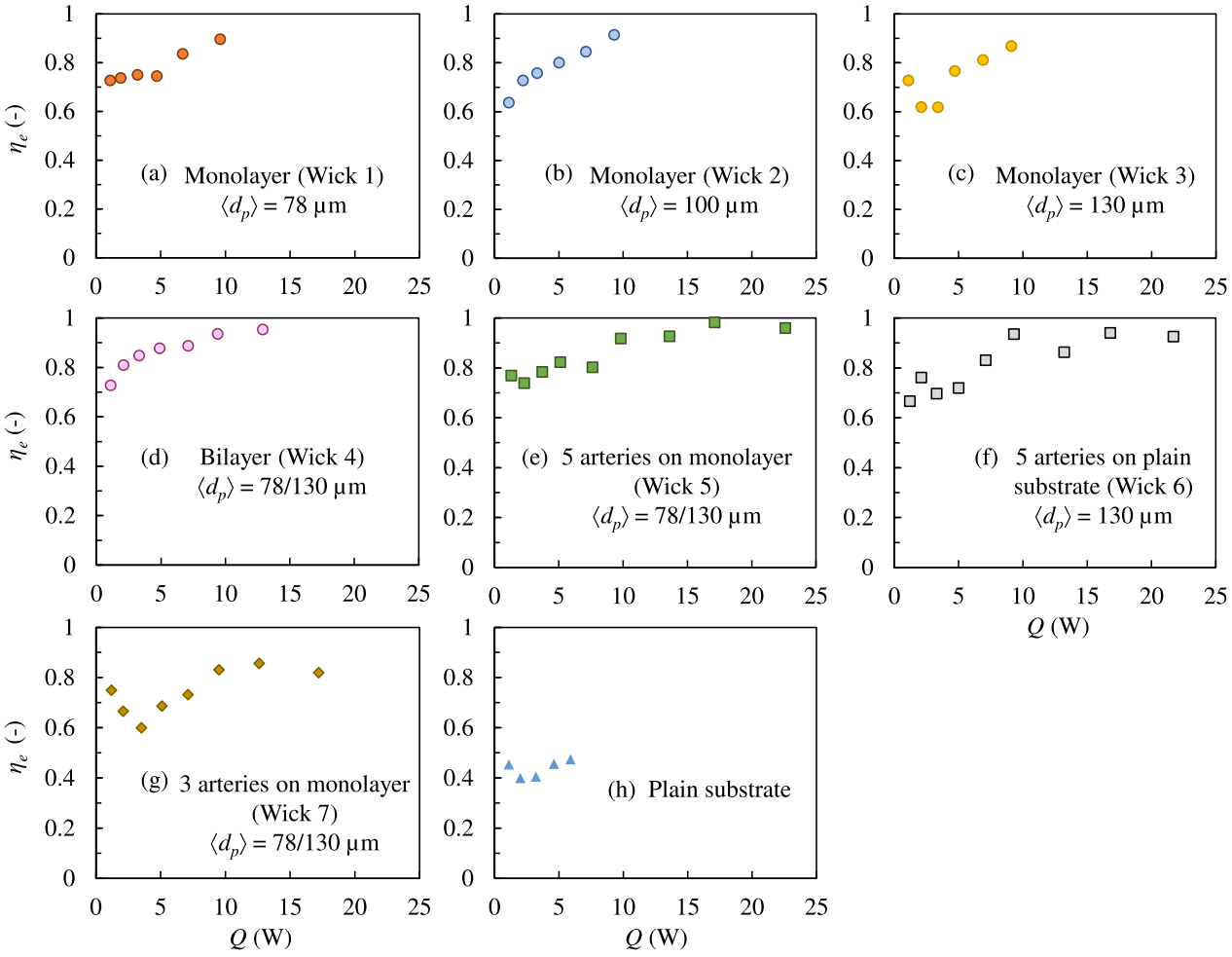

Fig. 7. Variations of the evaporation efficiency with respect to the heat flow rate, for various porous metasurface wicks (a–g) and the plain substrate (h).

is increased by a factor of 6.4 (= A_a/A_m). Second, the permeability increases by a factor of 1.5 (= K_a/K_m). Third, the effect of interartery meniscus rise increases by a factor of 1.6 [= $L_e/(L_e - h_a)$]. As a result, the increase in the predicted evaporation flux limit of Wick 5 is approximately 15 times higher than that of Wick 1. This increase in the predicted limit is consistent with the accelerated increase of evaporation flux with temperature, which differs from the behavior of Wick 1. The experimental values at high temperatures did not reach the predicted capillary-viscous limit. In Fig. 5(e), the dominant thermal resistance continues to prevail (no sign of capillary-viscous limit and jump, as seen for some other wicks, e.g., Wick 1). This discussion supports that the evaporation efficiency of Wick 5 nearly reached unity [Fig. 7(e)] and that almost all the supplied heat was utilized for evaporation. Therefore, the evaporation flux limit of Wick 5 was thermally controlled. By using capillary arteries with a proper design, we can avoid the capillary-viscous limit and enhance the evaporation flux.

6.3. Further enhancement of surface evaporation

The capillary arteries allow for the large amount of liquid supply; however the entire supply does not contribute to the evaporation flux because evaporation takes place only at the liquid-gas interface. So we examine the evaporation surface area of the 3-D wicks in comparison with that of a monolayer wick.

We approximate the evaporation surface area by considering the meniscus coverage as

$$A_e = W(h_{\max} - \delta_a - h_a) + 2(h_{\max} - \delta_a - h_a)\eta_f N_a \delta_a \,. \tag{10}$$

Here the maximum liquid height is $h_{max} = 2\sigma \cos\theta_c/\rho_l g r_{c,min}$. The hydrodynamic effect is included through the maximum capillary length adjustment allowing for pressure drop along δ_a. The interartery meniscus height is assumed to be $h_a = 2\sigma \cos\theta_c/\rho_l g W_g$. The fin efficiency η_f is introduced to consider the heat transfer effect, which is explained below. When $\delta_a = 0$ (i.e., a monolayer with no arteries), the interartery height h_a should be 0. Hence, we use $A_e(\delta_a = 0) = Wh_{\max}$. Then the surface-area enhancement is

$$\frac{A_e}{A_e(\delta_a = 0)} = \left(1 + \frac{2\eta_f \delta_a/W_a}{1 + W_g/W_a}\right)\left(1 - \frac{\delta_a/W_a}{h_{\max}/W_a} - \frac{2\sigma\cos\theta_c/W_a}{\rho_l g W_g/W_a}\right). \tag{11}$$

Since evaporation is the dominant heat transfer mechanism, we assume that the surface-area enhancement is equal to the heat flow ratio, that is, $A_e/A_e(\delta_a = 0) = Q_{lg}/Q_{lg}(\delta_a = 0)$. Thus the fin efficiency appeared in Eq. (10) can be treated using the following heat transfer analysis.

The fin efficiency for a rectangular fin of uniform cross section (with a perimeter P, a cross-sectional area A_c, and a fin surface area A_f, and a corrected fin length L_c) is given as $\eta_f = (\tanh mL_c)/mL_c$, where $m = (hP/kA_c)^{1/2}$, k is the thermal conductivity, and h is the heat transfer coefficient [37]. For the evaporation arteries, we have $P = 2(h_{max} - \delta_a - h_a)$, $A_c = W_a(h_{max} - \delta_a - h_a)$, $A_f = P\delta_a$, and $L_c = \delta_a + W_a/2$. Based on these relations, the fin efficiency of the evaporation arteries is

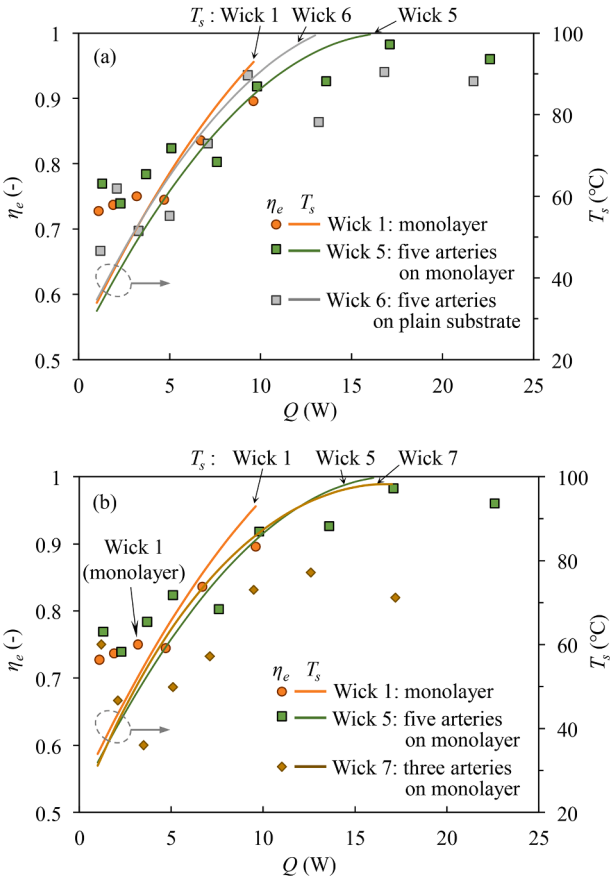

Fig. 8. Comparison of the evaporation efficiency and the wick surface temperature. (a) Wick 6 is compared with Wicks 1 and 5 to examine the role of the monolayer. (b) Wick 7 is compared with Wicks 1 and 5 to examine the influence of the interartery gap. The evaporation efficiencies are plotted using the symbols, and the surface temperatures are expressed by the curves.

$$\eta_f = \frac{1}{\delta_a/W_a + 1/2}\left(\frac{1}{2}\frac{k}{hW_a}\right)^{\frac{1}{2}} \tanh\left(2\frac{hW_a}{k}\right)^{\frac{1}{2}}\left(\frac{\delta_a}{W_a}+\frac{1}{2}\right). \tag{12}$$

Here we use the effective thermal conductivity of water-saturated arteries as [15],

$$k = k_f\left(\frac{k_s}{k_f}\right)^{0.280-0.757\log(\varepsilon)-0.057\log\left(k_s/k_f\right)}, \tag{13}$$

where k_f is the thermal conductivity of water, k_s is the thermal conductivity of copper, and ε is the porosity of capillary artery ($\varepsilon = 0.4$ is assumed for the random packing of spherical particles [27]). The fin efficiency calculation using Eq. (12) requires the heat transfer coefficient. Since the heat transfer is dominated by surface evaporation, the heat flow rate is the product of the liquid flow rate and the heat of vaporization ($\dot{M}_{l,a}\,\Delta h_{lg}$). So, the cooling from the artery surface is the thermal effect which represents the evaporation enhancement. The heat transfer coefficient is assumed using the mass flow rate in the arteries as,

$$h = \frac{\dot{M}_{l,a}\Delta h_{lg}}{A_c(T_s - T_\infty)}. \tag{14}$$

Note that only the conductive heat transfer in the arteries is considered, despite the existence of liquid flow. Using the experimentally obtained evaporation rate, we determined the Péclet number, which is defined as $\mathrm{Pe} = u_l\delta_a/\alpha_l$, where α_l is the thermal diffusivity, and u_l is the liquid flow velocity estimated from the evaporation rate [38]. For Wick 5, we have $\mathrm{Pe} < 0.1$; thus, we can neglect the convection effect in dealing with the fin efficiency.

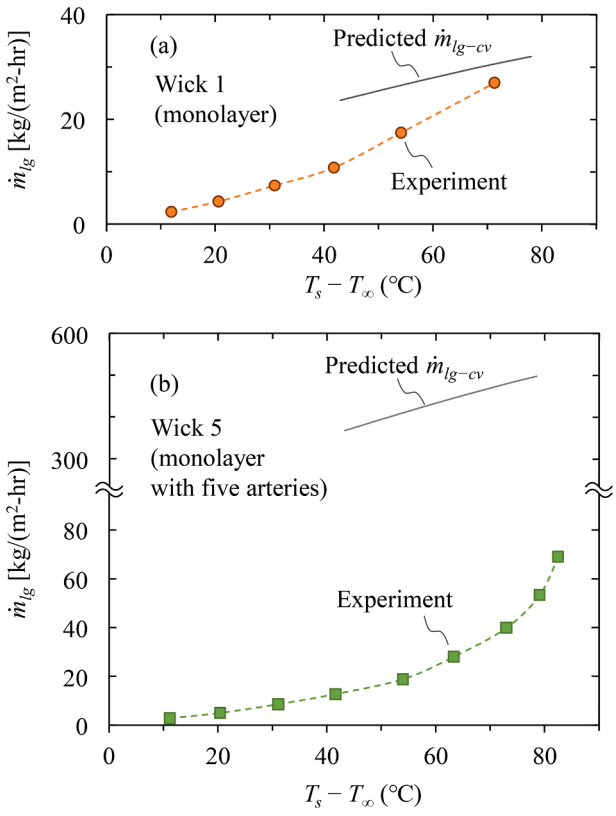

Fig. 9. Variation of the predicted capillary-viscous evaporation flux limit with respect to the wick surface temperature, up to the saturation temperature: (a) Wick 1 and (b) Wick 5. The experimental results are also shown and are below the predicted capillary-viscous limit.

The predicted heat flow ratio $Q_{lg}/Q_{lg}(\delta_a = 0)$ is shown in Fig. 10, as a function of the artery length-to-width ratio δ_a/W_a. The curves are drawn for several values of the interartery gap to the artery width ratio; $W_g/W_a = 0.5$, 1, 3, and 10. Here we assume the fabrication limit as $W_g/W_a = 0.5$, considering the practical conditions in the fabrication of 3-D wicks.

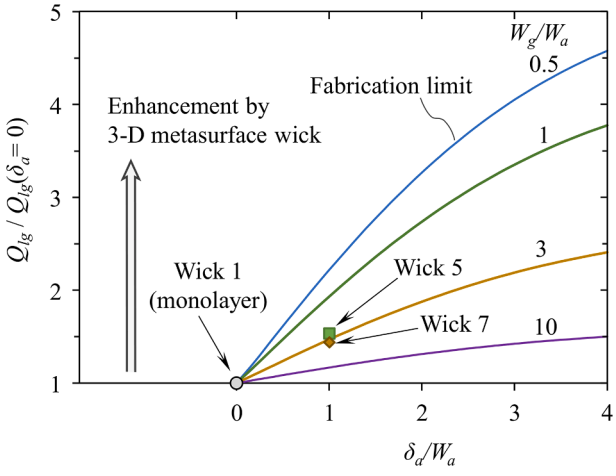

Fig. 10. Variations of the predicted heat flow ratio, showing the evaporation enhancement using 3-D metasurfaces, as a function of the artery length-to-width ratio δ_a/W_a. The results for several values of the interartery gap to the artery width ratio W_g/W_a are shown. The experimental results are also shown. The hydrodynamic effect is included through the maximum capillary height adjustment, allowing for the pressure drop along δ_a. The thermal effect through the fin efficiency, which decreases for a large artery length δ_a, is also included.

The experimental results for Wick 5 ($\delta_a/W_a = 1$ and $W_g/W_a = 1$) and Wick 7 ($\delta_a/W_a = 1$ and $W_g/W_a = 3$) are also plotted, using the result of Wick 1 as a reference. As the artery length increases, the heat flow ratio begins to increase. At the same time, the fin efficiency decreases with δ_a and suppresses the heat flow enhancement, as indicated by Eq. (12). This results in the plateau in the heat flow ratio at large artery lengths.

The measured and predicted heat flow ratio Q_{lg}/Q_{lg} ($\delta_a = 0$) for Wick 7 are 1.44 and 1.47, respectively. Therefore, Wick 7 has a performance comparable to the predicted performance, with about 50% enhancement. The test result for Wick 5 (i.e., 1.53) is below the predicted value (i.e., 1.93), and this may be due to fabrication defects such as any gap or spacing between the monolayer and the arteries. Also, here we used a small number of unit cells (up to five), however, in practice and in future studies a larger number should be used. The demonstrated enhancement of surface evaporation can be useful in developing efficient water evaporators for example using solar energy [2,3]; open-system water--vapor generation using solar heat source requires improved thermal efficiency and is one of the potential applications of the proposed wick evaporators [4]. Other potential application in the thermal engineering is the evaporator used in adsorption chiller systems [39,40]. The proposed metasurfaces allow for the control and tailoring of the surface structures for optimal evaporation.

The results show that the surface-area leading to larger heat flow has a potential of substantial increase by using 3-D metasurface wick. Still wick 5 achieves over 50% enhancement over Wick 1, and further enhancement is expected using a longer artery length and a smaller interartery gap. Hence the optimization of geometrical parameters of 3-D wicks is desirable. Also, the proposed wicks should be used with higher energy densities than used here, to investigate potential applications in, for example, the concentrated solar systems [41,42].

7. Conclusions

Vapor production via surface evaporation is used across many technologies, and its enhancement and efficiency are continuously pursued. Here the use of porous metasurfaces for capillary enhancement of the surface evaporation is proposed and implemented using sintered copper particles and evaporation of water with direct heating. The porous metasurfaces are made of a uniform, thin wick (mono- or bilayer wick) and fin-like arteries that act as extended surfaces for evaporation. The monolayer and bilayer wicks are susceptible to partial dryout at high heat flow rates, manifested by substantial increase in the thermal resistance, i.e., limited heat flow range and evaporation rate. These limitations are predicted with the capillary-viscous analysis of the viscous liquid flow, capillarity, gravity, and surface evaporation. The 3-D metasurface structures with unit-cell based arteries allow for extra evaporation surface and suppression of the partial dryout, thus expanding the range of heat flow and evaporation rates. The fabricated and tested 3-D porous metasurface combining the monolayer and the irrigating arteries, with an interartery spacing to artery width ratio of unity and an artery thickness to width ratio of unity, results in 50% evaporation enhancement over the monolayer-only surface. This evaporation enhancement by the extended surface (i.e., irrigating arteries) is also controlled by the capillary-viscous and heat transfer limits. The thermal-hydraulics analysis of this 3-D porous metasurface predicts that the arteries with the smallest interartery gap and long length result in the highest evaporation enhancement. Due to limited variations in the fabricated-tested metasurface wicks, further work should extend these to verify the analytical model prediction to smaller interartery spacing and thicker arteries.

CRediT authorship contribution statement

Yuki Kameya: Conceptualization, Writing – original draft, Validation, Funding acquisition, Supervision. **Yuya Takahashi:** Investigation, Validation. **Massoud Kaviany:** Methodology, Writing – original draft, Writing – review & editing.

Declaration of Competing Interest

The authors declare the following financial interests/personal relationships which may be considered as potential competing interests

Yuki Kameya reports financial support was provided by Japan Society for the Promotion of Science.

Data availability

Data will be made available on request.

Acknowledgment

This research was supported by JSPS KAKENHI Grant Numbers 20K05406 and 23K04652.

Appendix A: Experimental setup

The schematic drawing of the experimental setup described in Section 5 is shown in Fig. A.1. The wick structure was only on one side of the substrate and the other side was exposed to air with no evaporation. So, the evaporation proceeded dominantly at the wick surface. This reasoning is supported by the low thermal resistance of the wick evaporator (Fig. 5).

To support the interpretation of the experimental results, we estimated heat loss from the substrate back side to air by natural convection. Using the laminar-regime correlation for natural convection of air over vertical plate [37]

$$\mathrm{Nu}_L = \frac{hL}{k} = 0.59\ \mathrm{Ra}_L^{1/4}, \tag{A.1}$$

$$\mathrm{Ra}_L = \frac{g\beta(T_s - T_\infty)L^3}{\nu\alpha}, \tag{A.2}$$

and assuming an ideal gas gives $\beta = 1/T$. For the wick substrate (10 × 50 mm), $L = 0.050$ m, $T_s = 100\ ^\circ$C, $T_\infty = 22\ ^\circ$C, $\beta = 3.0 \times 10^{-3}\ \mathrm{K}^{-1}$, $\alpha = 29.9 \times 10^{-6}\ \mathrm{m}^2/\mathrm{s}$, $\nu = 20.9 \times 10^{-6}\ \mathrm{m}^2/\mathrm{s}$, and $g = 9.8\ \mathrm{m/s}^2$, we obtain $\mathrm{Ra}_L = 4.6 \times 10^5$. With $k = 30 \times 10^{-3}$ W/m-K and $\mathrm{Nu}_L = 15.4$, we have $h = 9.26\ \mathrm{W/m}^2\text{-K}$, which results in $Q_{loss} = Ah(T_s - T_\infty) = 0.36$ W. The heat flow rate of Wick 5 exceeds 20 W, so the substrate heat loss to air is negligibly small.

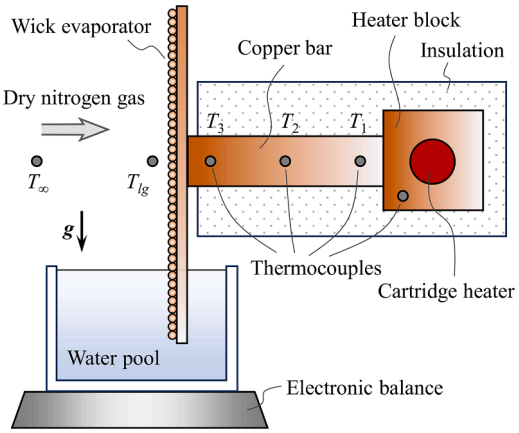

Fig. A.1. Schematic of the experimental setup (not to scale). The rate of water pool mass loss and the temperatures in the copper bar are measured to determine the evaporation rate and its associated rate of phase-change heat, respectively.

Appendix B: Uncertainty estimation of experimental results

Assuming one-dimensional conduction in the copper bar, the linear regression provides the heat flux q as [36],

$$q = -k\frac{N\sum x_i T_i - \sum x_i \sum T_i}{N\sum {x_i}^2 - \left(\sum x_i\right)^2}, \tag{B.1}$$

where k is the thermal conductivity of copper, N is the number of data points, x is the location of thermocouple along the copper bar, and T is the measured temperature. Since three thermocouples ($N = 3$) were used, $i = 1, 2, 3$.

Using the uncertainties in temperature and thermocouple location ($U_T = \pm 0.5$ °C and $U_x = \pm 0.4$ mm, respectively), the standard uncertainty propagation gives the heat flux uncertainty as [34],

$${U_q}^2 = \sum_i \left(\frac{\partial q}{\partial T_i}\right)^2 {U_T}^2 + \sum_i \left(\frac{\partial q}{\partial x_i}\right)^2 {U_x}^2 . \tag{B.2}$$

The maximum uncertainty in heat flux is 30%. This is shown with error bar in Fig. 5.

The substrate surface temperature T_s is extrapolated as

$$T_s = T_3 - \frac{q}{k}(x_s - x_3), \tag{B.3}$$

where the index of 3 indicates the thermocouple closest to the wick (Fig. A.1), and x_s is the location of the wick substrate surface. The uncertainty of the surface temperature is given as [34],

$${U_{T_s}}^2 = \left(\frac{\partial T_s}{\partial T_3}\right)^2 {U_T}^2 + \left(\frac{\partial T_s}{\partial q}\right)^2 {U_q}^2 + \left(\frac{\partial T_s}{\partial x_3}\right)^2 {U_x}^2 . \tag{B.4}$$

The specific thermal resistance $A_h R$ is

$$A_h R = \frac{\Delta T}{q} = \frac{T_s - T_{lg}}{q} , \tag{B.5}$$

where T_{lg} is the liquid-vapor interfacial saturation temperature. The uncertainty of the thermal resistance is

$${U_{A_h R}}^2 = \left(\frac{\partial A_h R}{\partial T_s}\right)^2 {U_{T_s}}^2 + \left(\frac{\partial A_h R}{\partial T_{lg}}\right)^2 {U_T}^2 + \left(\frac{\partial A_h R}{\partial q}\right)^2 {U_q}^2 . \tag{B.6}$$

The estimated uncertainties are reflected in Fig. 5, and the maximum error in $A_h R$ is 53%.

References

[1] A.E. Kabeel, et al., Solar powered hybrid desalination system using a novel evaporative humidification tower: Experimental investigation, Sol. Energy Mater. Sol. Cells 248 (2022), 112012.
[2] N. Benz, T. Beikircher, High efficiency evacuated flat-plate solar collector for process steam production, Sol. Energy 65 (1999) 111.
[3] D. Gao, et al., A novel direct steam generation system based on the high-vacuum insulated flat plate solar collector, Renew Energy 197 (2022) 966.
[4] L. Xu, et al., Performance of solar mid-temperature evacuated tube collector for steam generation, Sol. Energy 183 (2019) 162–172.

[5] G. Peng, et al., A study on the upper limit efficiency of solar still by optimizing the mass transfer, Appl. Therm. Eng. 213 (2022), 118664.
[6] C. Chen, et al., Challenges and opportunities for solar evaporation, Joule 3 (2019) 683.
[7] Y. Pang, et al., Solar-thermal water evaporation: a review, ACS Energy Lett. 5 (2020) 437.
[8] P. Tao, et al., Solar-driven interfacial evaporation, Nat. Energy 3 (2018) 1031.
[9] Y.L. Wang, et al., Cost-effective and eco-friendly laser-processed cotton paper for high-performance solar evaporation, Sol. Energy Mater. Sol. Cells 218 (2020), 110693.
[10] B. Bai, et al., A high efficiency solar steam generation system with using residual heat to enhance steam escape, Desalination 491 (2020), 114382.
[11] Y. Xu, et al., Low cost, facile, environmentally friendly all biomass-based squid ink-starch hydrogel for efficient solar-steam generation, J. Mater. Chem. A 8 (2020) 24108.
[12] G. Peng, et al., Low-cost high-efficiency solar steam generator by combining thin film evaporation and heat localization, Appl. Therm. Eng. 143 (2018) 1079.
[13] G. Vaartstra, et al., Capillary-fed, thin film evaporation devices, J. Appl. Phys. 128 (2020) 30901.
[14] J. Wang, I. Catton, Enhanced evaporation heat transfer in triangular grooves covered with a thin fine porous layer, Appl. Therm. Eng. 21 (2001) 1721.
[15] G.S. Hwang, et al., Multi-artery heat pipe spreader: Experiment, Int. J. Heat Mass Transfer 53 (2010) 2662–2669.
[16] Y.S. Ju, et al., Planar vapor chamber with hybrid evaporator wicks for the thermal management of high-heat-flux and high-power optoelectronic devices, Int. J. Heat Mass Transfer 60 (2013) 163–169.
[17] M. Egbo, G. Hwang, Phase-change heat transfer of bare surface evaporator with phase-separating wick in downward facing orientation, Int. J. Heat Mass Transfer 173 (2021), 121206.
[18] Y. Sun, et al., Hierarchically 3D-textured copper surfaces with enhanced wicking properties for high-power cooling, Appl. Therm. Eng. 178 (2020), 115650.
[19] Q. Li, et al., Fabrication and capillary characterization of multi-scale micro-grooved wicks with sintered copper powder, Int. Comm. Heat Mass Transfer 121 (2021), 105123.
[20] J.-C. Yu, et al., High-performance electrodeposited copper wicks for heat-spreading vapor chambers, Appl. Therm. Eng. 228 (2023), 120495.
[21] G.S. Hwang, et al., Multi-artery heat-pipe spreader: Lateral liquid supply, Int. J. Heat Mass Transfer 54 (2011) 2334.
[22] M. Kim, M. Kaviany, Multi-artery heat-pipe spreader: monolayer-wick receding meniscus transitions and optimal performance, Int. J. Heat Mass Transfer 112 (2017) 343–353.
[23] M. Lee, C. Park, Receding liquid level in evaporator wick and capillary limit of loop thermosyphon, Int. J. Heat Mass Transfer 146 (2020), 118870.
[24] A. Lininger, A.Y. Zhu, J.-S. Park, G. Palermo, S. Chatterjee, J. Boyd, F. Capasso, G. Strangi, Optical properties of metasurfaces infiltrated with liquid crystals, Proc. Natl. Acad. Sci. 117 (34) (2020) 20390–20396.
[25] J. Ferreira, M. Kaviany, Direct simulation of flow-boiling crisis and its porous-metasurface control for very large dryout limit, Int. J. Heat Mass Transfer 194 (2022), 123051.
[26] Z. Chen, S. Modak, M. Kaviany, R. Bonner, Direct simulations of biphilic-surface condensation: optimized size effects, Front. Heat Mass Transfer 14 (2020) 1–11.
[27] M. Kaviany, Principles of Heat Transfer in Porous Media, 2nd ed., Springer, 1995.
[28] D.H. Min, et al., Multi-artery, heat pipe spreader, Int. J. Heat Mass Transfer 52 (2009) 629–635.
[29] J.C. Berg, An Introduction to Interfaces & Colloids, World Scientific, 2010.
[30] Y. Kameya, et al., Hydrophilic coating of copper particle monolayer wicks for enhanced passive water transport, Energies 13 (2020) 3294.
[31] T.K. Kim, et al., Flow-boiling canopy wick capillary-viscous limit, Int. J. Heat Mass Transfer 181 (2021), 121999.
[32] N.D. Denkov, et al., Two-dimensional crystallization, Nature 361 (1993) 26.
[33] N. Albu, et al., Bimodal, thin wick structures for high heat flux two-phase thermal control systems, in: Proc. 49th Int. Conf. Env. Sys., 2019. ICES-2010-206.
[34] S. Sudhakar, et al., Experimental investigation of boiling regimes in a capillary-fed two-layer evaporator wick, Int. J. Heat Mass Transf. 135 (2019) 1335.
[35] M. Egbo, et al., Phase-change heat transfer of sintered-particle wick in downward facing orientation: Particle size and wick thickness effects, Int. J. Heat Mass Transf. 155 (2020), 119840.
[36] J.R. Taylor, An Introduction to Error Analysis: The Study of Uncertainties in Physical Measurements, 2nd ed., University Science Books, 1997.
[37] F.P. Incropera, et al., Principles of Heat and Mass Transfer, Global edition, John Wiley & Sons, Singapore, 2017.
[38] M. Kaviany, Essentials of Heat Transfer, Cambridge University Press, 2011.
[39] K. Sztekler, et al., Experimental study of three-bed adsorption chiller with desalination function, Energies 13 (21) (2020) 5827.
[40] K. Sztekler, et al., Performance evaluation of a single-stage two-bed adsorption chiller with desalination function, J. Energy Res. Tech. 143 (2021), 082101.
[41] Y. Xu, et al., Heat-concentrating solar steam generation and salt extraction based on water-repellent germanium nanoparticles-coated oxidized copper foams, Sol. Energy Mater. Sol. Cells 230 (2021), 111191.
[42] A.K. Singh, Samsher, Techno-environ-economic-energy-exergy-matrices performance analysis of evacuated annulus tube with modified parabolic concentrator assisted single slope solar desalination system, J. Clean. Prod. 332 (2022), 129996.